Journal of Materials Chemistry A

PAPER

Cite this: J. Mater. Chem. A, 2015, 3, 13365

6 2015
A 20 2015

D I: 10.1039/ 5 01703

www.rsc.org/MaterialsA

Optimizing the thermoelectric performance of low-temperature SnSe compounds by electronic structure design

A. J. H , L. L , H. , . B. , J.- . L *. F.

fi - - (*ZT*) ~2.62
923 K, *ZT* 750 K . I
- B z
ZT *a*- *c*- 67.5 K
b- 2.57 z
$n \sim 3.6 \times 10^{19}$ $^{-3}$. I –

I. Introduction

Thermoelectric (TE) materials and devices have been receiving much attention over the past few decades due to their capabilities for direct and reversible conversion between electrical energy and heat energy.[1–10] The search for proper TE materials with high conversion efficiency is important for developing advanced TE technologies.[11] For a TE device, the thermal power PF = $S^2\sigma$ and the dimensionless figure of merit $ZT = S^2\sigma T/\kappa_{tot}$ are two core parameters,[1] where S, T, σ, κ_{tot}, κ_l, and κ_e represent, respectively, the Seebeck coefficient, absolute temperature, electrical conductivity, total thermal conductivity, and lattice and electronic components of κ_{tot} ($\kappa_{tot} = \kappa_l + \kappa_e$). Nevertheless, for realistic TE materials, simultaneously achieving high PF and low κ_{tot} remains a contradictory issue due to the competing dependences of the parameters (S, σ, κ_l, and κ_e) on chemical and electronic structures,[5,9,10] making maximization of the TE performance extremely challenging. Because of such complexities, theoretical predictions from the full-scale first-principles calculations have been of interest in guiding TE materials synthesis.

It has been proposed that a combination of electronic crystal and phononic glass in one material is a promising approach.[1,3–7] This requires the simultaneous and delicate design of the crystalline and electronic structures. The electrical conductivity σ depends on the carrier density and mobility, which are both determined by electronic structure, while the Seebeck coefficient S is essentially determined by the gradient of density of states (DOS) of the conduction band near the Fermi level (chemical potential).[11] Surely, the lattice thermal conductivity κ_l can be substantially suppressed by modulating the material microstructure,[3] but the electronic thermal conductivity κ_e is again highly dependent on the electronic structure. In a general sense, one is in a good position to optimize the TE performance of a material by tentatively designing the electro- and thermo-transport behaviors based on the electronic structure. In other words, electronic structure engineering has become a major branch of TE materials science.

To engineer the transport behaviors, one of the effective and often-employed approaches is to modulate the carrier density (n) by chemical substitution and charge doping (thus varying the chemical potential μ) without seriously distorting the topology of the electronic structure. Such carrier density modulation may lift or lower the Fermi level (*i.e.* μ) so that the ZT can be optimized. A common strategy is to choose some TE parent compounds with one or more outstanding TE parameters and then improve the other parameters in order to reach optimized PF and ZT values. Along this line, a series of parent compounds have been explored, followed by extensive investigations on the consequence of various doping trials for each compound.

Recent studies[9,12–14] revealed that selenium-based compounds are promising TE candidates. While polycrystalline β-CuAgSe exhibited very low κ_{tot} (<0.5 W m^{-1} K^{-1}) and the ZT reaches up to ~0.95 at 623 K (ref. 14), polycrystalline Cu_2Se was found to have a ZT value as high as 1.5 at T = 1000 K.[12] Surprisingly, the single-crystal SnSe compound was reported to have a ZT value as high as 2.62 along the b-axis and 2.30 along the c-axis at T ~923 K.[9] These values represent the highest ones reported so far, and thus allow SnSe to be a good platform for exploring the possibilities for even better TE performance.

[a]Laboratory of Solid State Microstructures and Innovation Center of Advanced Microstructures, Nanjing University, Nanjing 210093, China. E-mail: liujm@nju.edu.cn; Tel: +86 25 83596595

[b]Department of Physics and TcSUH, University of Houston, Houston, TX 77204, USA

Similar to Cu_2Se, the SnSe compound has two phases.[15,16] The high-T phase possesses ultralow κ_l (<0.25 W m^{-1} K^{-1} at T > 800 K) and moderate PF values, thus leading to surprisingly high ZT values.[9] Very differently, the low-T phase, however, shows much lower TE properties, and its ZT value along the b-axis is only ~1.0 at T ~750 K, the transition point between the two phases.

Considering the requirement for intermediate-T applications and the fact that the low-T SnSe compound has high Seebeck coefficient (S > 500 μV K^{-1} at T < 675 K and S > 400 μV K^{-1} at T = 300–750 K), the promotion of its overall TE performance is highly desired. Experimentally reported carrier density of SnSe alloys in the intermediate T range is relatively low ($n \sim 10^{18}$ cm^{-3}),[9] which leaves sufficient space for carrier density modulation by means of low-level carrier doping.

II. Approach and theory

In this work, we intend to perform a full-scale first-principles electronic structure calculation on the low-T SnSe phase and subsequently evaluate the electro- and thermo-transport properties at finite T by means of the semi-classic Boltzmann transport theory. In this scheme, all the thermodynamic properties relevant to electron transport can be calculated quantitatively so long as chemical potential μ (or doping carrier density n) is given. Along this line, one is allowed to investigate the consequence of charge/carrier doping (low level) without seriously distorting the topology of the electronic structure. Similar schemes have been extensively employed for TE materials design and performance optimization.[17–20] Our calculations indeed predict the significant impact of carrier density variation on the TE properties of low-T SnSe phase.

We start from the experimentally determined crystal structure of the low-T SnSe phase.[15] It has the space group *Pnma* (#62), as shown in Fig. 1, and the lattice constants are a = 11.58 Å, b = 4.22 Å, and c = 4.40 Å. The Sn and Se atoms are located on two different planes with the dihedral angle of ~20°. We employ the density functional theory (DFT) scheme with the full-potential linearized augmented plane-wave (LAPW) method implemented.[21] The WIEN2k package can offer high-precision and accurate calculations on electronic structure with relatively low efficiency. The exchange and correlation interactions are described using the generalized gradient approximation (GGA) and the Perdew–Burke–Ernzerhof (PBE) functional modified by the Becke–Johnson potential (mBJ).[22] The mBJ is a local approximation of an atomic "exact-exchange" potential and a screening term. The mBJ method allows the calculation of band gaps with accuracy similar to the very expensive GW calculations[22] and can improve the band gap in sp-bonded semiconductors.[23] The muffin-tin radii are set as 2.5 a.u. for both Sn and Se atoms with a well-converged basis set determined by $R_{MT} \times K_n = 7.0$, corresponding to 5907 plane waves. In our calculations, we fix the lattice symmetry and lattice constants, and then all atoms in the conventional cell are allowed to relax sufficiently until the minimization of forces is less than 0.5 mRy per a.u.

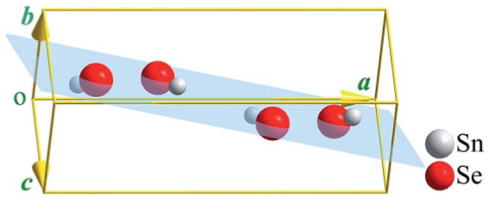

Fig. 1 A -T

Given the whole set of electronic structure data and varying μ, we employ the semi-classic Boltzmann transport theory to calculate the electro- and thermo-transport behaviors. The calculated transport coefficients are found to be converged using a shifted 20 × 55 × 53 k mesh. The original k mesh is interpolated onto a mesh five times as k dense. All of the calculations are implemented by solving the Boltzmann transport equation with the constant relaxation time approximation.[24] In details, the electrical conductivity tensors and electronic thermal conductivity tensors at non-zero electric current are obtained by the following equations:[24]

$$\sigma_{\alpha\beta}(T,\mu) = \frac{1}{\Omega}\int \sigma_{\alpha\beta}(\varepsilon)\left[-\frac{\partial f}{\partial \varepsilon}\right]d\varepsilon \quad (1)$$

$$\kappa^0_{\alpha\beta}(T,\mu) = \frac{1}{e^2T\Omega}\int \sigma_{\alpha\beta}(\varepsilon)(\varepsilon-\mu)^2\left[-\frac{\partial f}{\partial \varepsilon}\right]d\varepsilon \quad (2)$$

where e, Ω, ε, and f are the electron charge (e), reciprocal space volume (Ω), carrier energy (ε), and Fermi distribution function (f), respectively. The conductivity tensors $\sigma_{\alpha\beta}$ can be expressed as:

$$\sigma_{\alpha\beta}(\varepsilon) = \frac{e^2\tau}{N}\sum_{i,k} v_\alpha v_\beta \frac{\delta(\varepsilon-\varepsilon_{i,k})}{d\varepsilon} \quad (3)$$

where τ and v_α (v_β) are the relaxation time and electron group velocity; k is the wave-vector. In the standard procedure, the S and κ_e at zero electric current can be obtained:

$$S_{ij}(T,\mu) = (\sigma^{-1})_{\alpha i}c_{\alpha j} \quad (4)$$

$$\kappa_{ij} = \kappa^0_{ij} - Tc_{i\beta}(\sigma^{-1})_{\alpha\beta}c_{\alpha j} \quad (5)$$

where

$$c_{\alpha\beta}(T,\mu) = \frac{1}{eT\Omega}\int \sigma_{\alpha\beta}(\varepsilon)(\varepsilon-\mu)\left[-\frac{\partial f}{\partial \varepsilon}\right]d\varepsilon. \quad (6)$$

It should be mentioned that relaxation time τ is weakly dependent on the band index and k-direction, and is thus spatially anisotropic for most cases. However, this dependence is quite trivial and can be neglected safely without much damage to the results, even in the quantitative sense. Earlier studies[25,26] did indicate that the τ is orientation-independent for most materials, *i.e.* approximately isotropic. Even for superconducting cuprates whose electrical conduction is known to be anisotropic, this relaxation time remains almost isotropic.

Therefore, realistic calculations often take this approximation, although these properties may be spatially anisotropic.

As is well known, doping carrier density n is given by:

$$n = n_0 - \int f(\varepsilon, \mu, T)D(\varepsilon)\mathrm{d}\varepsilon \quad (7)$$

where n_0 is the valence electron number and $D(\varepsilon)$ is the total DOS as a function of ε as evaluated from the electronic structure. There is a one-to-one correspondence between doping carrier density n and chemical potential μ at a given T. To this stage, a self-consistent calculation based on the Boltzmann transport theory is immediate, and no details of the practical calculation procedure are repeated here.

III. Results and discussion

A. Electronic structures

The calculated band structures and DOS along the high symmetry lines are shown in Fig. 2. The reciprocal space a^*, b^*, and c^* axes are parallel to the real space a-, b-, and c-axes. All energies are referenced to the middle of the band gap. It can be seen that the conduction band minimum (CBM) is located at the Γ point, and there is a local CBM at (0.000, 0.329, 0.000) along the Γ–Y line. The first and second valence band maximums (VBMs) are located at (0.000, 0.000, 0.354) and (0.000, 0.000, 0.444) along the Γ–Z line. There is the third VBM at (0.000, 0.316, 0.000) along the Γ–Y line, implying two indirect band gaps, $E_g = 0.849$ eV and 0.862 eV, along the Γ–Y line. Along the Γ–Z line, there are also two indirect band gaps, $E_g = 0.842$ eV and 0.828 eV. The similar gaps allow similar transport properties along the a- and b-axes. As is well known for an indirect bandgap semiconductor, electrons cannot shift from the VBM to the CMB without momentum change. Fig. 2 shows that the VBM and CBM have nearly equal momentum at gap ②. Namely, electrons are more easily excited into the conduction band at band gap ② than those at other band gaps.

It is noted that gap ② (E_g = 0.862 eV) almost equals the previously measured value of 0.86 eV.[9] We then focus on the upper part of the highest valence band. The dispersion along the Γ–Z line is greater than that along the planar A–Z. The flat part of the highest-valence band near the VBM is beneficial for high Seebeck, and the conductivity is determined mostly by the steep band. In fact, earlier work[27–30] indicated that a mixture of the heavy and light bands near the valence edge is favorable for high TE performance, because the light band allows good electrical conduction and the heavy band benefits the high Seebeck coefficient. In addition, Fig. 2 shows that the total DOS increases more rapidly near the VBM than that near the CBM. The major DOS contribution to the CBM comes from the Sn atoms, while the Se atoms contribute more to the DOS near the VBM.

The orbital-decomposed band structures are presented in Fig. 3(a) and (b), where the coarseness of curves scales the DOS intensity. It is seen that the VBM mainly comes from the Se 4p states, and the Sn 5p states only have weak contribution. This suggests that the p-type doping at the Sn site will increase the carrier density so as to improve the electrical conductivity, while the VBM shape can be roughly maintained so as to keep the high Seebeck coefficient. The projected DOS in the [−10.0 eV, 10.0 eV] interval is shown in Fig. 3(c). A comparison of Fig. 3(c) with 2 allows us to conclude that the bands from the Fermi level to 5.0 eV are mainly from the Sn 5p and Se 4p states, while the bands from −5.0 eV to the Fermi level primarily come from the Se 4p states. The highest bonding peaks near the VBM show the characteristics of the Se 4p electrons but also contain contributions from the Sn 5s electrons, implying the weak s–p hybridization between the Sn and Se atoms. Such s–p hybridization can lead to dramatic DOS variation near the VBM, which is favorable for a high Seebeck coefficient.

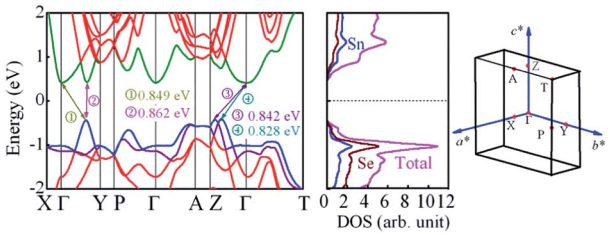

Fig. 2 C D D

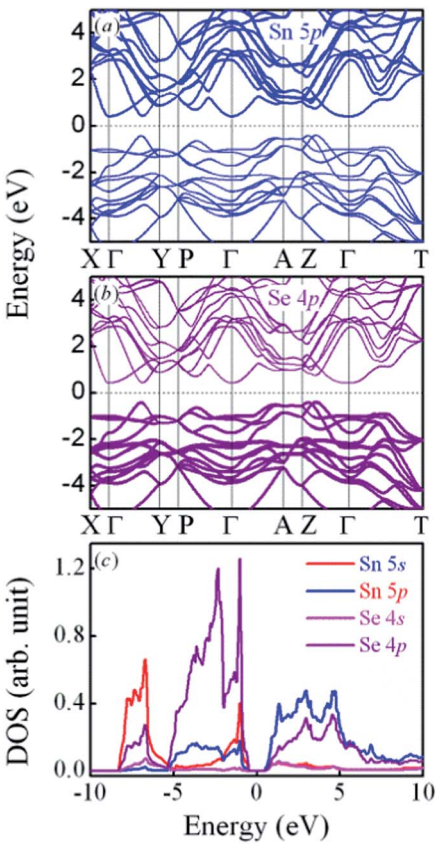

Fig. 3 C - .5 ( ) 4 ( ).I j D 5 , 5 , 4 , 4 ( ).

We also calculate the electron density and charge density difference on the Se–Se–Se plane (schematically shown in Fig. 1 by the shadow plane), as displayed in Fig. 4(a) and (b), respectively. The Sn–Se bond has a weak covalent component, which again confirms the s–p hybridization between the Se 4p and Sn 5s. The weak tendency for Se atoms to accumulate charge from the surrounding Sn atoms can also be seen in Fig. 4(b). It is thus suggested that the bond between the Sn and Se atoms is more or less of mixed ionic–covalent nature.

B. Thermoelectric properties

Subsequently, we investigate the electro- and thermo-transport behaviors. In Fig. 5(a)–(e) are plotted several calculated parameters as a function of n, respectively, along the three major axes at $T = 675$ K. The $S(n)$ curves show the single-peaked pattern and the peak location and height shift along different major axes. The peak values of $S(n)$ along the a-, b- and c-axes reach up to 544.07, 690.37, and 655.13 μV K^{-1}, respectively, at $n \sim 9.8 \times 10^{19}$, 2.3×10^{19}, and 2.3×10^{19} cm^{-3}.

To calculate other parameters, relaxation time τ is needed, but extracting its value from the *ab initio* calculation is still challenging. Usually, the constant relaxation time approximation is used,[31,32] and we take $\tau = 0.5 \times 10^{-14}$ s in the present calculations. The $\sigma(n)$ dependences along the three axes are all monotonous at high doping level with small differences along the b- and c-axes, but the $\sigma(n)$ along the a-axis decreases with increasing n at low doping level. It can be seen from Fig. 5(a) that the $\sigma(n)$ along the b-axis is much larger than along the a-axis at high doping level. $S(n)$ and $\sigma(n)$ exhibit opposite dependences, resulting in the PF peaks along these axes roughly at $n \sim 10^{20}$ to 10^{21} cm^{-3}. The PF along the b-axis is about twice as large as that along the c-axis and almost ten times larger than that along the a-axis. The $\kappa_e(n)$ along all three axes is very sensitive to n. Fig. 5(d) presents that the κ_e along the b- and c-axes first decrease and then increase with increasing n. However, the κ_e along the a-axis first increases, and then decreases, and again rapidly increases with increasing n. In

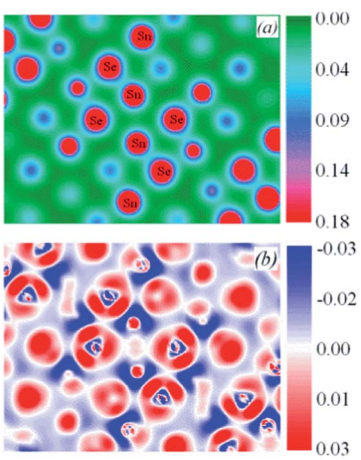

Fig. 4 C . . . . . (.) . . . . . ff . . – – . ( ).

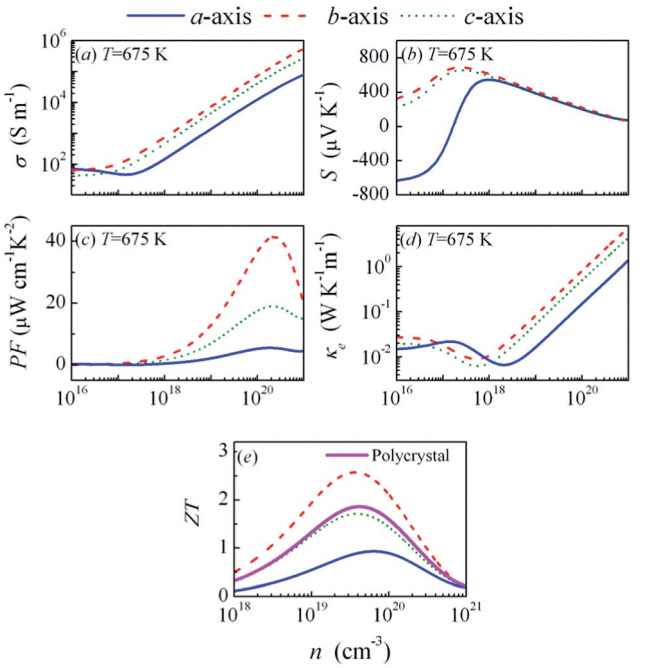

Fig. 5 C . . I E . . . S, σ, κ , F, . ZT .. . . . . - . . . . n T = 675 K, . ZT(n) . . . . . .

essence, the $\kappa_e(n)$ dependence is determined by the band structure of SnSe crystals.

As an example, the evaluated $ZT(n)$ curves along the three major axes at $T = 675$ K for the p-type doped systems are presented in Fig. 5(e), where measured κ_l values were taken from ref. 9. One sees that ZT is sensitive to the p-type carrier density, and a variation of n over two orders of magnitude is sufficient to modulate the ZT between the minimal and maximal. The $ZT(n)$ dependence is also anisotropic, yielding the relation $ZT_{b\text{-axis}} > ZT_{c\text{-axis}} > ZT_{a\text{-axis}}$, in agreement with experimental results.[9] The predicted highest ZT value of ~2.57 occurs at the p-type carrier density $n \sim 3.6 \times 10^{19}$ cm^{-3} along the b-axis, which needs experimental checking. We also predict the $ZT(n)$ of polycrystalline SnSe at the same temperature, as shown in Fig. 5(e). The highest ZT value can reach up to 1.86 at the p-type carrier density $n \sim 4.2 \times 10^{19}$ cm^{-3}.

C. Comparison with experiments

Finally, we compare our calculated data with measured data. So far, measured S, σ, and, κ_{tot} data along the three major axes of SnSe single crystals as a function of T are available.[9] For such a comparison, one needs measured $n(T)$ or $\mu(T)$ data for our calculations. Given the data in ref. 9 and the assumption of constant n ($=5 \times 10^{17}$ cm^{-3}) over the whole T range, the as-evaluated $S(T)$ and $\sigma(T)$ data are plotted in Fig. 6(a)–(f), focusing on the T-range from 300 K to 700 K. The calculated data coincide reasonably well with measured data along all the three axes, although the discrepancy becomes slightly remarkable at both extremes of the T range, particularly for $\sigma(T)$ along the b- and c-axes. The discrepancy is believed to most likely originate from the assumption of a constant relaxation time. In

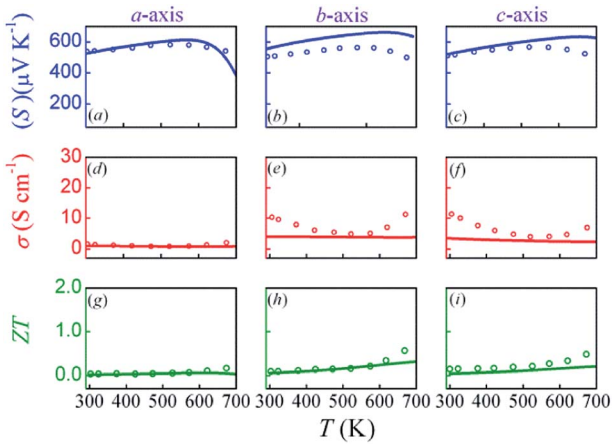

Fig. 6 E [illegible] E [illegible] S ([illegible]), σ ([illegible]), [illegible] ZT ([illegible]) [illegible] T. [illegible] 9.

addition, we extract the measured $\kappa_{\text{tot}}(T)$ data in ref. 9 to evaluate the $ZT(T)$ data, and the results are presented in Fig. 6(g)–(i) in comparison with measured $ZT(T)$ data.[9] Again, we see consistency between the calculated and measured ZT data, particularly in the low-T range.

The capability of the present computational scheme may be highly appreciated considering the current status of quantitative predictions for TE performances. It allows comprehensive design and evaluation of the TE performance for a realistic material. One can always start from the stoichiometric compound for electronic structure calculation, and then optimize the TE parameters by carefully tuning the chemical potential on condition of relatively low level doping so that the electronic structure topology remains qualitatively unchanged. This strategy is no doubt helpful for guiding the practical synthesis and substitution/doping processes for better TE materials and performance.

IV. Summary

In summary, we have calculated the electronic structure and TE properties of the low-T SnSe compound using the first-principles calculations plus the semi-classic Boltzmann transport theory. It is revealed that the high Seebeck coefficient and good electrical conductivity are attributed to the s–p hybridization and the mixed heavy-light band structure near the VBM. It is predicted that proper modulation of the chemical potential or p-type carrier density can remarkably enhance the power factor PF and figure-of-merit factor ZT. The calculated results are well consistent with experimental data reported recently. When the p-type carrier density is enhanced to $\sim 3.6 \times 10^{19}$ cm^{-3}, optimal ZT values up to ~2.57 along the b-axis at $T = 675$ K are predicted.

Acknowledgements

This work is supported by the National 973 Projects of China (Grant no. 2015CB654602), the Natural Science Foundation of China (Grant no. 51431006), and "Solid State Solar Thermal Energy Conversion Center (S^{3}TEC)", an Energy Frontier Research Center funded by the U.S. Department of Energy, Office of Science, Office of Basic Energy Science under award number DE-SC0001299.

Notes and references

1 T. M. Tritt and M. A. Subramanian, *Mater. Res. Soc. Bull.*, 2006, **31**, 188.
2 Y. L. Pei, H. J. Wu, J. H. Sui, J. Li, D. Berardan, C. Barreteau, L. Pan, N. Dragoe, W. S. Liu, J. Q. He and L. D. Zhao, *Energy Environ. Sci.*, 2013, **6**, 1750.
3 B. Poudel, Q. Hao, Y. Ma, Y. C. Lan, A. Minnich, B. Yu, X. Yan, D. Z. Wang, A. Muto, D. Vashaee, X. Y. Chen, J.-M. Liu, M. S. Dresselhaus, G. Chen and Z. F. Ren, *Science*, 2008, **320**, 634.
4 J. P. Heremans, V. Jovovic, E. S. Toberer, A. Saramat, K. Kurosaki, A. Charoenphakdee, S. Yamanaka and G. J. Snyder, *Science*, 2008, **321**, 554.
5 G. J. Snyder and E. S. Toberer, *Nat. Mater.*, 2008, **7**, 105.
6 M. S. Dresselhaus, G. Chen, M. Y. Tang, R. G. Yang, H. Lee, D. Z. Wang, Z. F. Ren, J.-P. Fleurial and P. Gogna, *Adv. Mater.*, 2007, **19**, 1043.
7 J. P. Heremans, M. S. Dresselhaus, L. E. Bell and D. T. Morelli, *Nat. Nanotechnol.*, 2013, **8**, 471.
8 V. P. Dravid and M. G. Kanatzidis, *Energy Environ. Sci.*, 2014, **7**, 251.
9 L. D. Zhao, S. H. Lo, Y. S. Zhang, H. Sun, G. J. Tan, C. Uher, C. Wolverton, V. P. Dravid and M. G. Kanatzidis, *Nature*, 2014, **508**, 373.
10 G. J. Snyder and E. S. Toberer, *Nat. Mater.*, 2008, **7**, 105.
11 F. Loff, *Semiconductor Thermoelements and Thermoelectric Cooling*, Infosearch Publishers, London, 1957.
12 H. L. Liu, X. Shi, F. F. Xu, L. L. Zhang, W. Q. Zhang, L. D. Chen, Q. Li, C. Uher, T. Day and G. J. Snyder, *Nat. Mater.*, 2012, **11**, 422.
13 S. Ishiwata, Y. Shiomi, J. S. Lee, M. S. Bahramy, T. Suzuki, M. Uchida, R. Arita, Y. Taguchi and Y. Tokura, *Nat. Mater.*, 2013, **12**, 512.
14 A. J. Hong, L. Li, X. H. Zhou, Q. Y. He, W. S. Liu, Z. B. Yan, J.-M. Liu and Z. F. Ren, *Solid State Ionics*, 2014, **261**, 21.
15 T. Chattopadhyay, J. Pannetier and H. G. Vonschnering, *J. Phys. Chem. Solids*, 1986, **47**, 879.
16 W. J. Baumgardner, J. J. Choi, Y.-F. Lim and T. Hanrath, *J. Am. Chem. Soc.*, 2010, **132**, 9519.
17 V. K. Gudelli, V. Kanchana, G. Vaitheeswaran, A. Svane and N. E. Christensen, *J. Appl. Phys.*, 2013, **114**, 223707.
18 K. P. Ong, D. J. Singh and P. Wu, *Phys. Rev. B: Condens. Matter Mater. Phys.*, 2011, **83**, 115110.
19 D. F. Zou, S. H. Xie, Y. Y. Liu, J. G. Lin and J. Y. Li, *J. Mater.Chem. A*, 2013, **1**, 8888.
20 T. J. Scheidemantel, C. Ambrosch-Draxl, T. Thonhauser, J. V. Badding and J. O. Sofo, *Phys. Rev. B: Condens. Matter Mater. Phys.*, 2003, **68**, 125210.
21 K. Schwarz, P. Blaha and G. K. H. Madsen, *Comput. Phys. Commun.*, 2002, **147**, 71.

22 J. P. Perdew, K. Burke and M. Ernzerhof, *Phys. Rev. Lett.*, 1996, **77**, 3865.
23 J. M. Yang, G. B. Zhang, G. Yang, C. Wang and Y. X. Wang, *J. Alloys Compd.*, 2015, **644**, 615.
24 G. K. H. Madsen and D. J. Singh, *Comput. Phys. Commun.*, 2006, **175**, 67.
25 P. B. Allen, W. E. Pickett and H. Krakauer, *Phys. Rev. B: Condens. Matter Mater. Phys.*, 1988, **37**, 7482.
26 W. W. Schulz, P. B. Allen and N. Trivedi, *Phys. Rev. B: Condens. Matter Mater. Phys.*, 1992, **45**, 10886.
27 D. Parker and D. J. Singh, *Phys. Rev. B: Condens. Matter Mater. Phys.*, 2012, **85**, 125209.
28 Y. L. Yan and Y. X. Wang, *J. Mater. Chem.*, 2011, **21**, 12497.
29 D. J. Singh and I. I. Mazin, *Phys. Rev. B: Condens. Matter Mater. Phys.*, 1997, **56**, R1650.
30 A. F. May, D. J. Singh and G. J. Snyder, *Phys. Rev. B: Condens. Matter Mater. Phys.*, 2009, **79**, 153101.
31 M.-S. Lee, F. P. Poudeu and S. D. Mahanti, *Phys. Rev. B: Condens. Matter Mater. Phys.*, 2011, **83**, 085204.
32 Y. L. Yan and Y. X. Wang, *J. Mater. Chem.*, 2011, **21**, 12497.

